WILEY-VCH

Stretchable ITO-free Organic Solar Cells with Intrinsic Anti-reflection Substrate for High-efficiency Outdoor and Indoor Energy Harvesting

*Jiaming Huang[1, 2], Zhiwei Ren[1], Yaokang Zhang[3], Kuan Liu[1], Hengkai Zhang[1,2], Hua Tang[1], Cenqi Yan[1], Zijian Zheng[3] and Gang Li[1, 2,]**

J. Huang, Dr. Z. Ren, Dr. K. Liu, H. Zhang, H. Tang, Dr. C. Yan, and Prof. G. Li
Department of Electronic and Information Engineering, Research Institute for Smart Energy (RISE), The Hong Kong Polytechnic University, Hung Hom, Kowloon, Hong Kong, China.
E-mail: gang.w.li@polyu.edu.hk

J. Huang, H. Zhang, and Prof. G. Li
The Hong Kong Polytechnic University Shenzhen Research Institute, Shenzhen 518057, China.

Dr. Y. Zhang, Prof. Z. Zheng
Laboratory for Advanced Interfacial Materials and Devices, Institute of Textiles and Clothing, The Hong Kong Polytechnic University, Hung Hom, Kowloon, Hong Kong, China.

Keywords: Stretchable photovoltaic electronics; Anti-reflection; ITO-free; Texturing stretchable substrates; Outdoor and Indoor application

Flexible photovoltaic devices are promising candidates for triggering the Internet of Things (IoT). However, the power conversion efficiencies (PCEs) of flexible organic photovoltaic (OPV) devices with high conductivity poly(3,4-ethylene dioxythiophene):polystyrene sulfonate (PEDOT:PSS) electrodes on plastic are lagging behind the rigid devices due to the low transmittance of polyethylene terephthalate (PET)/PEDOT:PSS. Moreover, the poor stretchability of the commonly used plastic substrates largely hinders the practical application of wearable devices. Herein, a novel stretchable indium tin oxide (ITO)-free OPV device with a surface-texturing polydimethylsiloxane (PDMS) substrate for outdoor strong- and indoor dim-light energy harvesting is reported. The high diffuse transmittance and haze effect of the substrate enable stretchable ITO-free devices, yielding a high PCE of 15.3% under 1-sun illumination. More excitingly, the stretchable device based on textured PDMS/PEDOT:PSS maintained a comparable PCE of 20.5% (20.8% for the rigid device) under indoor light illumination. Notably, the stretchable device is much more insensitive to the light direction, still maintaining 38.5% of the initial PCE at an extremely small incident angle of 10° (16.3% for

glass/ITO-based counterpart). Our texturing stretchable substrate provides a new direction for achieving high performance and enhanced light utilization for the stretchable and wearable light-harvesting device, suitable for the application in both indoor and outdoor scenarios.

Portable and wearable electronics have experienced rapid development, triggering tremendous demands for highly efficient power sources featuring robustness and mechanical flexibility.[1-9] Organic photovoltaics (OPVs) offer an ideal combination of light-weight, cost-effectiveness, intrinsic flexibility, transparency, and scalable fabrication.[10-20] At present, the power conversion efficiencies (PCEs) of OPVs have been boosted from approximately 10% in the fullerene acceptor era to over 17% due to the innovative evolution of non-fullerene acceptors (e.g., ITIC, Y6).[21-30] Intensive research efforts have been targeted at flexible OPVs, in particular indium tin oxide (ITO)-free flexible transparent electrodes (FTEs), such as conducting polymer, metal nanowires, and graphene, which enabled a PCE of 15%.[31-39]

A reliable FTE should possess high optical transmittance, high conductivity, reduced surface roughness, and excellent stability. Although positive progress (high-efficiency and good mechanical stability) has been demonstrated in flexible OPVs with plastic substrates, such as polyethylene terephthalate (PET), polyimides (PI), and perylene[40-43], the high Young's modulus of PET (2–2.7 GPa) and PI (3.1 GPa) substantially limit their practical application in the field of stretchable electronics.[44-46] For example, PET film experiences irretrievable deformation after complete folding. PDMS elastomer has been highlighted as a promising candidate for various bendable and stretchable applications, due to its merits including low Young's modulus (3 MPa), high specific power, and excellent biocompatibility.[47] Anti-reflection coating (ARC) and surface texture patterns offer efficient light-trapping with an increased optical pathway, resulting in high light utilization. This very favorable feature is seamlessly integrated into our surface-textured flexible ITO-free substrate-based OPVs.

Furthermore, the application of OPVs in indoor dim-light energy harvesting is highly promising.[48-53] Indoor dim-light can be directly converted into electrical energy to power smart electronic devices with low-energy consumption. In comparison with solar irradiation, indoor dim-light sources demonstrate distinct intensities and spectra. Most reported high-efficiency indoor OPVs were obtained from rigid glass/ITO electrode devices. More importantly, unlike collimated sunlight, indoor light is not directional. In such low-light conditions, sufficiently using light to maximize the output power is a critical problem.

In this study, a high-efficiency stretchable ITO-free OPV device with a surface-textured substrate for indoor dim-light energy harvesting is reported. The surface texture formation of the stretchable PDMS substrate is a simple, facile, and scalable reduplication process using commercial 3M abrasive paper. The devices with surface-textured PDMS/PEDOT:PSS substrates delivers decent bendability and stretchability. The intrinsic high diffuse transmittance and haze effect of our substrate lead to excellent anti-reflection properties. The devices with the surface-textured stretchable PDMS/PEDOT:PSS transparent electrode show a high PCE of 15.3% under 1-sun illumination (AM 1.5G), with a higher J_{SC} than the flat counterpart. Moreover, the devices with surface-textured stretchable ITO-free substrates demonstrate an impressive PCE of 20.5%, which is comparable to that of the glass/ITO substrate (20.8%) under indoor dim-light conditions. The devices with surface-textured stretchable ITO-free substrates exhibit a superior indoor performance over those with rigid ITO glass substrates at small incident angles (higher by 2.5 times at 10°) owing to their increased incident light pathways that sufficiently improve indoor dim-light utilization. Novel stretchable surface-textured substrates offer a new direction for achieving high performance and enhanced light energy harvesting.

Figure 1a shows a schematic diagram of the fabrication of flexible OPV devices. Previously, many attempts have been made to construct regular nano- or micro-structures using laser interference lithography, nanostructure dry etching technology, or surface texture

duplication from biomimetics such as rose petals.[54-59] Here, we use commercial 3M abrasive papers with mesh numbers of 2k, 6k, and 10k as templates that are low-cost and easily scalable. The device fabrication process consists of three main steps. In the first step, the PDMS precursor was prepared according to the literature and spin-coated onto the abrasive paper attached to a glass, followed by PDMS curing at room temperature for two days. The obtained PDMS substrate had a flat front surface and patterned back surface, with a total thickness of approximately 300 μm. The cured PDMS substrates were then peeled off from the template and reattached onto a Teflon holder for further processing. Step two was the fabrication of the transparent electrode of PEDOT:PSS by acid treatment. High conductivity PEDOT:PSS (PH1000) was first doped with a surfactant, followed by acid treatment. The Capstone™ FS-3100 surfactant doping increases the wettability of PH1000 on the PDMS substrate.[60] Here, weak acetic acid was used to prevent PDMS from being corroded by a strong acid. Due to the low boiling point of acetic acid, the post-acid PEDOT:PSS films can be directly annealed at 100 °C removing the residual acid without water washing. Step three is the typical fabrication of OPVs covered by another PDMS layer. The device structure is also shown in **Figure 1a**.

The 3D laser scanning microscope was first used to investigate the surface morphology of the 3M abrasive papers with different mesh numbers. **Figure 1b** shows that, as mesh number increased from 2k, 6k, to 10k, the size of the surface microparticles also decreased. The surface roughness (R_a) obtained from the abrasive paper surface was 5.95 μm, 4.37 μm, and 0.75 μm, respectively. **Figure 1c** displays the surface of the PDMS films, which uniformly duplicated the negative surface morphology from abrasive papers, which we call 2k-, 6k-, and 10k-PDMS. The 2k-, 6k-, and 10k-PDMS showed R_a values of 6.18 μm, 5.60 μm, and 0.96 μm, consistent with the trend in the corresponding abrasive papers. Scanning electron microscopy (SEM) was employed to measure the size of the microparticles on abrasive papers and PDMS films, as depicted in **Figure S1 (Supporting Information)**. The average microparticle sizes estimated

from the SEM images were approximately 10 μm, 5 μm, and 1 μm for 2k, 6k, and 10k abrasive papers and PDMS films, respectively.

The optical properties of PDMS substrates were measured by ultraviolet-visible (UV–vis) spectroscopy with an integrating sphere. Diffuse transmittance is the ratio of the total amount of transmitted light in all directions to the total amount of incident light.[61] **Figure 2a** exhibits the diffuse transmittance of flat and patterned PDMS as well as glass, which is the substrate of the rigid OPV device. The flat PDMS (F-PDMS) film shows a clearly higher transmittance of 94% over the entire range of 350–800 nm than the benchmark glass. For the patterned substrate, 10k-PDMS shows the highest transmittance near 98% in the entire visible region, while the 6k- and 2k-PDMS show 96.5% and 94.5%, respectively. Moreover, the reflective index (1.41) of PDMS is lower than that of glass (1.52), indicating that less light would be lost (reflected) in the air-PDMS interface than in the air-glass interface case. This agrees with the reflectance spectra in **Figure 2b**, where all PDMS substrates exhibit lower reflectance (< 6%) than glass in the entire region. Furthermore, multiple reflections and refractions enabled by the surface microparticles of patterned PDMS can form a gradient-effective refractive-index profile,[62, 63] which further reduces the reflectance of PDMS to below 5%. 10k-PDMS showed the lowest reflectance of ≤ 4%, while 2k- and 6k-PDMS were ≤ 5%.[64, 65] The high transmittance and low reflectance enable suppressed light loss and enough light utilization to improve OPV efficiency.

The photonic flux density (PFD) was calculated using the following equation: $\mathrm{PFD}(\lambda) = \frac{I_S(\lambda)T(\lambda)}{hv}$ to estimate the number of photons transmitted across the substrates, where I_s (λ) is the solar irradiance spectra of AM 1.5G, T is the diffuse transmittance spectra, and hv is the photon energy. **Figure 2c** depicts the integral PFD versus wavelength based on PDMS and glass substrates. The highest photonic flux was achieved by 10k-PDMS, followed by the 6k-, 2k-, and F-PDMS substrates. The rigid glass substrate exhibited the lowest PFD values, indicating a high loss of incident light. Moreover, the values of solar weight transmittance (SWT) were

calculated to determine the utilization of solar photons using the following equation: $SWT = \frac{\int I_S(\lambda)T(\lambda)d\lambda}{\int I_S(\lambda)d\lambda}$. The PDMS-based substrates exhibited SWT values of 98.4%, 97.2%, 94.8%, and 94.3% for 10k-, 6k-, 2k-, and F-PDMS, respectively. For the rigid glass substrate, SWT was only 88.38%.

Transmission haze is the ratio of light with wide-angle scattering ($\geq$ 2.5°) to total transmitted light.[66] **Figure 2d** shows the transmittance haze of the substrates. Both F-PDMS and glass display the few scattered light and transmittance haze < 1%. The patterned PDMS substrates show high transmittance haze of over 90%, 88%, and 48% for 2k-, 6k-, and 10k-PDMS, respectively. PDMS substrates were first placed directly onto a paper to visualize the haze effect (**Figure 2e**). The logos on the paper were clearly observed. When the substrates were lifted and kept approximately 2.0 cm from the paper, the logos were still clearly observed through glass and F-PDMS. The logo under the 10k-PDMS became blurred but still could be recognized. In contrast, the logos under 6k- and 2k-PDMS become too hazy to recognize, consistent with the transmittance haze spectra result. Another method was also used to visualize haze behaviors. Laser beams with wavelengths of 530 and 650 nm were selected to generate a point on the wall (**Figure 2e**). The light spot was concentrated when the laser beam was transmitted through the glass or F-PDMS substrates, while it became dispersed through 10k-PDMS, indicating a mild haze effect. The central light spot entirely disappeared and was replaced with a diffused luminous area when the laser beam went through the 2k- and 6k-PDMS. This suggested that almost all the light paths were changed through multiple reflections and refractions, enabled by the surface pattern of these PDMS substrates. The mechanisms of light transmission through different substrates are illustrated in **Figure 2f**.

According to the Cassie–Baxter theory, surface wettability can be significantly influenced by the roughness of heterogeneous surfaces.[67] The contact angles of a water droplet on the glass and patterned surface of PDMS were measured and are shown in **Figure S2 (Supporting**

Information). The water contact angle (θ_{CA}) of glass was 84.99°, which is smaller than that of F-PDMS (103.14°). The 10k-PDMS sample showed a slightly larger θ_{CA} of 104.12° owing to the small microparticles. The 2k- and 6k-PDMS samples showed high hydrophobic behavior with θ_{CA}s of 141.91° and 132.12°, due to the relatively large microparticles. Such hydrophobic behavior on the back surface would benefit OPV device self-cleaning.

Conductive polymers poly (3,4-ethylene dioxythiophene):poly (styrene sulfonate) (PEDOT:PSS) were utilized as the transparent electrodes in our devices. Acid treatment was conducted to rearrange and remove the PSS by forming PSSH in the films. To avoid damage to the PDMS substrate, acetic acid was selected to treat the PEDOT:PSS films. The surface of the PDMS film after dipping in acetic acid for 10 min is shown in **Figure S3 (Supporting Information)**. No cracks or pinholes were observed on the surface. The PDMS substrate was still smooth and uniform after acid dipping, which is essential for a good OPV substrate. Ultraviolet photoelectron spectroscopy (UPS) was employed to detect the work function of the PDMS/PEDOT:PSS electrode (**Figure S4, Supporting Information**). The work function was ≈ -5.0 eV for the pristine PEDOT:PSS film and ≈ -4.9 eV with acetic acid dipping. X-ray photoelectron spectroscopy (XPS) was used to verify the composition of the PEDOT:PSS film. As seen in **Figure S5 (Supporting Information)**, compared to the pristine PEDOT:PSS film, the S peak of $-SO_3H$ in PSS decreased from 70.1% to 56.4% after acetic acid dipping. The surface morphologies of PDMS/PEDOT:PSS were investigated by atomic force microscopy (AFM). All the PEDOT:PSS films show low roughness with root mean square (RMS) of 1 to 1.5 nm (**Figure S6, Supporting Information**). The PEDOT:PSS FTE showed an average sheet resistance (R_{sh}) of 64 Ω/sq and conductivity (δ) of 2400 S/cm.

Figure 3a illustrates the optical transmittance of the PEDOT:PSS electrode based on PDMS substrates. From 350 to 550 nm, the transmittance of the F-PDMS/PEDOT:PSS substrate was clearly higher than that of glass/ITO. For PEDOT:PSS based on 2k-, 6k-, and 10k-PDMS, the transmittance in the entire 350–800 nm range was improved to over 84.6%,

86.6%, and 89.1%, and the highest values reached 91.8%, 93.3%, and 93.8% at 450 nm, respectively. The values of the figure of merit (FoM) were calculated using the following equations: $\mathrm{FoM}=\frac{\delta_{dc}}{\delta_{op(\lambda)}}=\frac{188.5}{R_{sh}\,(T_{(\lambda)}^{-0.5}-1)}$, where R_{sh} is 64 Ω/sq, and T is the transmittance of the substrate/transparent electrode at 550 nm. The calculated FoM values were 44.5, 57.0, 75.7, and 85.6 for F-, 2k-, 6k-, and 10k-PDMS/PEDOT: PSS, respectively. We note that, unlike the FoM calculation done in previous studies, which excluded the substrate transmission loss, our FoM calculation accounted for the transmittance loss of the substrates. Even with the substrate transmission loss, the FoM values of PDMS/PEDOT:PSS here are comparable to those in previous reports, indicating the suitability for OPV applications.[37, 68-70]

The OPV devices were fabricated with the configuration of substrate/FTEs/PEDOT:PSS (Al4083)/PM6:BTP-4Cl/PFN-Br/Ag, and the energy level diagram is shown in **Figure S7 (Supporting Information)**. The substrates were glass and PDMS for rigid and flexible devices, respectively. The full names and chemical structures of the active layer materials and interlayer materials are shown in the experimental section and **Figure S8 (Supporting Information)**. Moreover, the absorption of the PM6:BTP-4Cl blend film is also shown in **Figure S9 (Supporting Information)**. **Figure 3b** shows the *J*–*V* curves of the devices measured under AM 1.5G 100 mW·cm^{-2}. **Table 1** summarizes the corresponding photovoltaic parameters. The glass/ITO-based rigid device exhibited a high PCE of over 16.3% with an open-circuit voltage (V_{OC}) of 0.860 V, short-circuit current density (J_{SC}) of 25.4 mA·cm^{-2}, and fill factor (FF) of 75.1%, which is consistent with the previous literature.[22] The device based on F-PDMS/PEDOT:PSS showed a PCE of 14.2% with V_{OC} of 0.852 V, J_{SC} of 23.3 mA·cm^{-2}, and FF of 72.6%. In the devices based on patterned PDMS substrates, an improved J_{SC} was observed. Due to the high diffuse transmittance, the 10k-PDMS/PEDOT:PSS-based device showed an improved J_{SC} of 24.0 mA·cm^{-2} and a PCE of 14.7%. The high transmittance haze of 2k-PDMS enabled the OPV device to exhibit a PCE of 14.9% with a J_{SC} of 24.3 mA·cm^{-2}. The champion

device was obtained based on 6k-PDMS, which has both a high diffuse transmittance of over 97% and haze of over 85%. Finally, a high PCE of 15.3% with V_{OC} of 0.853 V, J_{SC} of 25.0 mA·cm^{-2}, and FF of 72.1% was observed, and is one of the highest efficiencies reported to date for flexible OPVs. To verify the function of the anti-reflection substrates, the PDMS films were attached onto the glass, and its performance was measured (**Table S1, Supporting Information**). The devices showed an obvious PCE improvement after laminating the textured PDMS films, as previously reported.[71-73] We noticed that the highest efficiency improvement was achieved based on 6k-PDMS, which exhibited both high diffused transmittance and haze effect, which is much less studied in transparent OPV so far. This PCE enhancement was attributed to the synergy of the anti-reflection and extended effective optical path lengths by haze[74], which enabled the higher photocurrent in a certain active layer thickness. For 2k- and 10k-PDMS, either low haze or low diffused transmittance impeded higher light utilization. The external quantum efficiency (EQE) measurement was used to investigate the photoresponse of the devices. **Figure 3c** and **Table 1** show the EQE spectra and corresponding calculated integral current density (J_{Cal}). The J_{Cal}*s* we obtained are consistent with that measured under AM 1.5G. All the PDMS/PEDOT:PSS-based devices showed higher EQE values than that of glass/ITO in the range of 300 to 450 nm, which is due to the high transmittance in the short-wavelength range. The EQE of the patterned PDMS-based devices was higher than that of the F-PDMS substrate throughout the range from 300 to 1000 nm, which indicates that the patterned PDMS substrates can improve the sunlight utilization regardless of the wavelength due to the haze effect. The main difference between glass/ITO-based devices and PDMS/PEDOT:PSS-based devices is attributed to FF, which is due to the electrode conductivity difference. This will be discussed in detail later.

Compared to previous flexible OPV substrates such as PET, the PDMS substrate offers more flexibility because of its low Young's modulus. After fully folding several times, PETs with obvious creases cannot recover, while PDMS shows no obvious crease (**Figure S10,**

Supporting Information). More importantly, the stretchability of PDMS provides a potential stretchable application. Therefore, the mechanical stabilities of PDMS/PEDOT:PSS-based electrodes and OPV devices were investigated (**Figure 3d–f**). The bending test was first conducted on the PDMS/PEDOT:PSS electrode. After bending 1000 times with a 1.5 cm radius, the R_{sh} of the electrode increased to 1.93 times larger than the initial value. However, the corresponding OPV device retained only 52.0% of the initial PCE after bending 1000 times. Such large PCE degradation is ascribed to Ag electrode damage because of the inevitable tensile set (stretch deformation) during the bending test operation. To release the strain on the Ag top electrode, a layer of PDMS was cured onto the surface of the OPVs and no apparent PCE degradation was observed. With PDMS encapsulation, after bending 1000 times, the device still retained 83% of the initial PCE. The stretching test was also applied to the PDMS-based device. Considering the low stretchability of the Ag electrode, a mild stretch ratio of approximately 8–10% was applied. The PDMS/PEDOT:PSS electrode exhibited a 1.7, 2.4, and 4.1 R/R_0 after 200, 500, and 1000 cycle times, respectively, indicating that the PDMS/PEDOT:PSS electrode is a candidate for stretchable OPV substrates. However, the device without PDMS encapsulation showed poor stretching stability, with approximately 30% of the initial PCE after 200 cycles. More cycle times would lead to the Ag electrode cracking or even delamination. After "encapsulating" by PDMS, the devices showed approximately double the stability of over 62% of the initial PCE after 200 cycle times. Considering the OPV structure, the polymer-based electrode, interlayer, and active layer have higher stretch tolerance than the Ag electrode. In this case, replacing the top metal with other electrodes, such as Ag NWs or PEDOT:PSS, would be an ideal method to improve the mechanical properties, especially the stretch stability.[75-78]

The photovoltaic performance of rigid and flexible devices was measured under indoor dim-light conditions. A warm white LED lamp with 2700 K color temperature, which is widely used in daily life, was employed as the indoor light source. An Ocean Optics spectrometer was used to determine the input power (P_{in}) from an LED lamp. In this study, light intensities of

500, 1000, and 1500 lx were achieved by adjusting the distance between the LED lamp and the device, covering the range of daily indoor lighting for different occasions.[79, 80] The conversion between input power and illuminance is shown in the Supporting Information. **Figure 4a** shows the input power spectra versus wavelength and the corresponding integral P_{in}. The calculated P_{in} values of 500, 1000, and 1500 lux were 158.0, 315.9, and 473.9 $\mu W \cdot cm^{-2}$, respectively. The corresponding photon flux values were calculated using the equation $E_\lambda = N_\lambda \cdot e \cdot h\nu$, where E_λ is the input power, N_λ is the photon flux, e is the elementary charge, h is the Planck constant, and ν is the light frequency. The estimated current density was calculated from the integration of photon flux and EQE spectra with the equation $J_{Cal} = e \int_0^\infty N_\lambda \cdot EQE_\lambda \cdot d\lambda$. **Figure 4b** shows the photon flux and calculated J_{SC} of the devices based on glass/ITO, F-, and 6k-PDMS/PEDOT:PSS electrodes. The photon flux N_λ and calculated J_{SC} based on other devices are shown in **Figure S13 (Supporting Information)**. **Figure 4c** displays the *J–V* curves of the rigid device under 500, 1000, and 1500 lux WLED. **Table 2** summarizes the corresponding device parameters. The *J–V* curves and parameters of other devices are summarized in **Figure S14 (Supporting Information)**. Under dim-light conditions, the glass/ITO-based device showed a decreased V_{OC} of 0.702–0.738 V compared to the V_{OC} of 0.860 under AM 1.5G. As the light intensity increases, both V_{OC} and FF improved slightly. Unlike the AM 1.5G condition, where the ratio of photocurrent to dark current is overwhelming, at low-light intensity conditions, the device dark current has a more significant impact on the current density. From 500 to 1500 lux, the influence of the dark current on the devices decreased, which might be the reason for the improved V_{OC} and FF. The J_{SC} improved proportionally as the light intensity increased from 500 to 1500 lux, consistent with the J_{Cal} from photon flux and EQE spectra. The following equation calculated the values of output power (P_{out}) and corresponding PCE: $P_{out} = V_{OC} \times J_{SC} \times FF$; $PCE\ (\%) = P_{out}/P_{in} \times 100\%$. Finally, the rigid devices based on glass/ITO showed 19.7%, 20.3%, and 20.8% PCE under 500, 1000, and 1500 lux, respectively.

The PCEs of the stretchable devices based on PDMS substrates and PEDOT:PSS electrodes were also tested under indoor light conditions. **Figure 4d–e** shows the *J–V* curves of the F-PDMS and 6k-PDMS-based devices, and **Table 2** summarizes the parameters of the devices. The data of all the devices in this work are shown in **Table S2 (Supporting Information)**. For the F-PDMS/PEDOT:PSS-based device, the PCE was 17.9% under 500 lux with a V_{OC} of 0.694 V, J_{SC} of 55.1 μA·cm^{-2}, and FF of 73.2%. The devices showed a higher PCE of 18.4% and 19.0% under 1000 and 1500 lux, with improved V_{OC} and FF. The 6k-PDMS/PEDOT:PSS-based device shows a higher PCE than the flat device, as expected, boosted by the higher transmittance of substrates as well as the haze effect. Under low-light illumination, all three parameters, $J_{SC,}$ V_{OC}, and FF, improved. The champion device of 6k-PDMS/PEDOT:PSS showed 19.4%, 19.9%, and 20.5% PCE under 500, 1000, and 1500 lux, respectively. Notably, even though the PDMS/PEDOT:PSS transparent electrode has lower conductivity than glass/ITO, leading to a lower PCE under AM 1.5G, it is encouraging to see that the 6k-PDMS/PEDOT:PSS-based stretchable OPV device can achieve a PCE almost equal to that of the rigid glass/ITO device. A similar enhancement is also seen in 2k- and 10k-PDMS/PEDOT:PSS-based devices.

To determine the performance difference between the glass/ITO- and PDMS/PEDOT:PSS-based devices under AM 1.5G and LED illumination, the *J–V* curves of the devices under dark conditions were measured (**Figure 4f**). The reversed saturated currents based on ITO and PEDOT:PSS electrodes with an applied voltage from -0.5 to 0 V are almost the same. This indicates that the reversed leakage current of PEDOT:PSS-based flexible devices is as low as that of the ITO-based rigid device. The forward conducting current of the ITO-based rigid device is higher than that of the PEDOT:PSS-based device, which is due to the conductivity difference. The ITO electrode's sheet resistance is approximately 10 Ω/sq, much lower than PEDOT:PSS (over 60 Ω/sq). The series resistance (R_s) and shunt resistance of devices (R_p) are calculated from the inverse of the slope of the dark *J–V* curves at the open-circuit point and short-circuit point, respectively, to analyze the diode behavior (**Table 1)**. The estimated R_p

values are 2.00, 1.92, 1.62, 2.06, and 1.81 kΩ·cm^2 for the devices based on glass/ITO, F-, 2k-, 6k-, and 10k-PDMS/PEDOT:PSS, respectively. All the R_p values were of the same order of magnitude and had less impact on the photovoltaic performance. For the R_s, PEDOT:PSS-based devices were almost 1.5 to two times larger than that of ITO-based devices because of the relatively low conductivity of transparent electrodes, which is the main reason for the decreased FF from 75% to 72% in the PDMS/PEDOT:PSS-based device under AM 1.5G. In this way, further improving the conductivity of a transparent electrode is important to eliminate the efficiency gap between rigid and flexible devices under 1-sun conditions.

The device performance under AM 1.5G and LED spectra with varied intensities was studied. The variation in V_{OC} versus light intensity is investigated (**Figure 4g)**. In the range of 1–100 mW·cm^{-2}, the light source used was simulated solar spectrum AM 1.5G, while the WLED was used below 1 mW·cm^{-2}. $V_{OC} \propto \frac{nkT}{q} \ln P_{in}$, where n is the ideality factor, k is the Boltzmann constant, T is the room temperature, and q is the elementary charge. The fitted slopes based on glass/ITO and PDMS/PEDOT:PSS were 1.08 and 1.07 kT/q. A similar ideality factor means no deep traps in ITO or PEDOT:PSS-based devices. Both devices show biomolecular recombination, which is dominated by the active layer. Compared to the high-intensity range, the ideality factors under the low-intensity range are larger due to the amplified impact from the trap and leakage current. The PDMS/PEDOT:PSS-based device exhibits an ideality factor of 1.36 versus 1.44 in the glass/ITO device. According to the equivalent-circuit model $V_{OC} = \frac{nkT}{q} \ln\left[1+\frac{J_{ph}}{J_0}\left(1-\frac{V_{OC}}{J_{ph}R_pA}\right)\right]$, similar n values could be explained by the similar R_p values of glass/ITO- and PDMS/PEDOT:PSS-based devices.[81]

Figure 4h displays the FF variation versus light intensity. When the light intensity decreases, both devices show increased FF first from 100 to 1 mW·cm^{-2} and then decreased FF under dim-light conditions (lower than 1 mW·cm^{-2}). The former FF increase is due to the decreased charge carrier recombination with lower P_{in}, while the latter FF decrease should be

ascribed to the larger ratio of dark current to photogenerated current. As mentioned before, there is a performance gap between rigid and flexible devices under 100 mW·cm^{-2}. However, as the light intensity decreased, the difference between these two devices decreased. The FF gap was almost eliminated when P_{in} was < 1 mW·cm^{-2}. To explain this, an equivalent-circuit model was considered to simulate the FF variation in the ITO and PEDOT:PSS-based device under AM 1.5G and indoor light conditions (**Figure S15, Supporting Information**). The following empirical equation illustrates the impact of R_s and R_p on FF: $FF_s=FF_0(1-1.1r_s)+\frac{r_s^2}{5.4}$; $FF_p=FF_0(1-\frac{V_{OC}+0.7}{V_{OC}}\frac{FF_0}{r_p})$, where $r_s=\frac{R_s}{R_{CH}}$, $r_p=\frac{R_p}{R_{CH}}$, $R_{CH}=\frac{V_{MP}}{I_{MP}}\approx\frac{V_{OC}}{I_{SC}}$.[82] FF_0 is the theoretical FF limit, using 0 R_s and infinite R_p. FF_s and FF_p are the FFs, which are affected by R_s or R_p. R_{CH} is the characteristic resistance of the devices at the maximum power point. As mentioned, the PEDOT:PSS-based device showed comparable R_p, but larger R_s compared to the ITO-based device. Under AM 1.5G, the intense light source provided a high level of current (I_{sc} and I_{MP}), leading to a small R_{CH}. In this case, the large r_s had a negative influence on FF intensity. However, a large r_p has a negligible effect on FF_p. Therefore, R_s was more important than R_p under AM 1.5G. The lower conductivity of PEDOT:PSS than the ITO electrode led to a high R_s and, finally, a low FF (72% vs. 75%). Under the dim-light condition (LED), the number of photons was two or three orders of magnitude lower than under AM 1.5G, which achieved a higher R_{CH}. Therefore, a very small r_s indicates that R_s has less impact on the FF. In contrast, the FF is dominated by r_p. The PEDOT:PSS-based device showed a comparable FF to the ITO device. Hence, the disadvantage of a relatively low conductivity PDEOT:PSS electrode can be overcome for indoor applications.

Theoretically, the solar cell panel should be set perpendicular to the incident light (θ) to achieve the highest output power. Solar cell panels are generally set with a tilt angle of 30° or 45°, considering the sun movement and the local latitude.[83, 84] A part of the light would be unavoidably lost when θ deviates from 90°. Moreover, unlike parallel sunlight, light from

indoor light sources such as LEDs and fluorescent lamps are divergent in nature. In this indoor case, improving the PCE at different θ values is critical for practical applications. **Figure 5** shows the photovoltaic parameters of devices based on glass/ITO and 6k-PDMS/PEDOT:PSS electrodes measured under different θ. A series of θ from 90° to 10°, with a step of 10° was studied for these solar cells. For the glass/ITO-based device under AM 1.5G, with the decreased θ, the V_{OC} was slightly decreased owing to the weaker input light in the perpendicular direction, which is consistent with the theoretical V_{OC} calculated from Lambert's cosine law on the photovoltage: $V_{OC}(\theta) = V_{OC}(0) + \frac{nkT}{q}\ln(\cos\theta)$.[85] The J_{SC} reduced intensity from an initial 25 mA·cm^{-2} to 5 mA·cm^{-2} with a 10° θ. The J_{SC} versus θ curve followed $J_{SC0}\cdot\cos\theta$ very well, indicating that the geometrical cosine loss was the dominant effect.[86] The FF value slightly improved as θ decreased. Therefore, the θ decrease from 90° to 10° led to an overall PCE drop from over 16% to 2.64% in glass/ITO-based devices. As a comparison, the devices based on PDMS-PEDOT:PSS showed a similar tendency of V_{OC} and FF with rigid devices under AM 1.5G. However, the J_{SC} exhibited different behavior. The normal J_{SC} of the 6k-PDMS/PEDOT:PSS-based device was slightly lower than that of a glass/ITO-based device with a θ of 90°. The flexible device showed a higher J_{SC} than the rigid device with θ lower than 70°. With the further reduced θ, the J_{SC} of flexible devices was more than two times higher than that of the rigid device. This is because of the extended effective optical path lengths, which enable light absorption by the photoactive materials. Therefore, the devices showed a PCE of 5.88% versus 2.64% for 6k-PDMS/PEDOT:PSS versus glass/ITO, respectively. Under indoor application (1000 lux white LED, 2700 K), the J_{SC}-θ dependence deviated from the geometrical cosine loss, which originates from the non-collimated nature of LED light. The 6k-PDMS/PEDOT:PSS-based device showed a nearly equal J_{SC} in the range of 90° to 70°. The decrease in FF with the increase in θ originates from the low-light intensity, which is consistent with the discussion above. Therefore, the 6k-PDMS/PEDOT:PSS-based devices maintained

nearly 40% of their initial PCE at an extremely large incident angle (10°), 2.5 times higher than the glass/ITO-based device PCE. Considering the practical situation for indoor application, the flexible OPV device based on textured PDMS/PEDOT:PSS clearly demonstrates advantages in light-harvesting over rigid glass/ITO based devices.

In summary, a novel intrinsic anti-reflection, high-transmission, and stretchable substrate was designed to construct highly efficient stretchable ITO-free organic solar cells. The stretchable substrate showed a high diffuse transmittance of over 95% and a transmittance haze of 88%, which can be simply duplicated from the surface texture of commercial 3M abrasive papers. A champion PCE of 15.3%, one of the highest efficiencies of the reported stretchable OPV device, was obtained by the device with a 6k-PDMS/PEDOT:PSS transparent ITO-free substrate. This is because our proposed surface-textured stretchable ITO-free substrates contribute to maximizing light utilization. Owing to the high EQE and shunt resistance, the devices with the surface-textured ITO-free stretchable substrates exhibited a similar PCE of 20.5% compared to that of the rigid devices (20.8%) under indoor application, despite the existence of a noticeable PCE difference from 16.3% to 15.3% under AM 1.5G. We concluded that the influence of the low conductivity PEDOT:PSS electrode in the surface-textured ITO-free stretchable device can be effectively minimized under indoor application. More importantly, the devices with the surface-textured ITO-free stretchable substrate showed significantly enhanced light utilization under different incident angles. Notably, the device with a surface-textured stretchable ITO-free substrate was 2.5 times higher than that of the rigid device under indoor light at an incident angle of 80°. Our proposed surface-textured stretchable substrates provide a new direction toward achieving high performance and enhanced light utilization for indoor dim light-harvesting applications.

Conflicts of interest

There are no conflicts to declare.

Acknowledgments

This work was supported by Research Grants Council of Hong Kong (Project Nos Project Nos 15320216, 15218517, C5037-18G), National Natural Science Foundation of China (51961165102), Shenzhen Science and Technology Innovation Commission (JCYJ20170413154602102), and the Hong Kong Polytechnic University Internal Research Funds: Project of Strategic Importance (1-ZE29), Sir Sze-yuen Chung Endowed Professorship Fund (8-8480), University Supporting Fund for Major Research (1-BBAS).

Reference

[1] P. Cheng, G. Li, X. Zhan and Y. Yang, *Nat. Photonics* 2018, **12**, 131-142.

[2] B. Tian, X. Zheng, T. J. Kempa, Y. Fang, N. Yu, G. Yu, J. Huang and C. M. Lieber, *Nature* 2007, **449**, 885-9.

[3] M. B. Schubert and J. H. Werner, *Mater. Today* 2006, **9**, 42-50.

[4] J. E. Carlé, M. Helgesen, O. Hagemann, M. Hösel, I. M. Heckler, E. Bundgaard, S. A. Gevorgyan, R. R. Søndergaard, M. Jørgensen, R. García-Valverde, S. Chaouki-Almagro, J. A. Villarejo and F. C. Krebs, *Joule* 2017, **1**, 274-289.

[5] S. A. Hashemi, S. Ramakrishna and A. G. Aberle, *Energy Environ. Sci.* 2020, **13**, 685-743.

[6] H. Kimura, K. Fukuda, H. Jinno, S. Park, M. Saito, I. Osaka, K. Takimiya, S. Umezu and T. Someya, *Adv. Mater.* 2019, **31**, 1808033.

[7] C. Wang, X. Li, H. Hu, L. Zhang, Z. Huang, M. Lin, Z. Zhang, Z. Yin, B. Huang, H. Gong, S. Bhaskaran, Y. Gu, M. Makihata, Y. Guo, Y. Lei, Y. Chen, C. Wang, Y. Li, T. Zhang, Z. Chen, A. P. Pisano, L. Zhang, Q. Zhou and S. Xu, *Nat. Biomed. Eng.* 2018, **2**, 687-695.

[8] S. Park, S. W. Heo, W. Lee, D. Inoue, Z. Jiang, K. Yu, H. Jinno, D. Hashizume, M. Sekino, T. Yokota, K. Fukuda, K. Tajima and T. Someya, *Nature* 2018, **561**, 516-521.

[9] H. Jinno, K. Fukuda, X. Xu, S. Park, Y. Suzuki, M. Koizumi, T. Yokota, I. Osaka, K.

Takimiya and T. Someya, *Nat. Energy* 2017, **2**, 780-785.

[10] C. Yan, S. Barlow, Z. Wang, H. Yan, A. K. Y. Jen, S. R. Marder and X. Zhan, *Nat. Rev. Mater.* 2018, **3**, 18003.

[11] L. Meng, Y. Zhang, X. Wan, C. Li, X. Zhang, Y. Wang, X. Ke, Z. Xiao, L. Ding, R. Xia, H.-L. Yip, Y. Cao and Y. Chen, *Science* 2018, **361**, 5.

[12] G. Yu, J. Gao, J. C. Hummelen, F. Wudl and A. J. Heeger, *Science* 1995, **270**, 3.

[13] Y. Lin, J. Wang, Z. G. Zhang, H. Bai, Y. Li, D. Zhu and X. Zhan, *Adv. Mater.* 2015, **27**, 1170-4.

[14] J. Yuan, Y. Zhang, L. Zhou, G. Zhang, H.-L. Yip, T.-K. Lau, X. Lu, C. Zhu, H. Peng, P. A. Johnson, M. Leclerc, Y. Cao, J. Ulanski, Y. Li and Y. Zou, *Joule* 2019, **3**, 1140-1151.

[15] W. Song, X. Fan, B. Xu, F. Yan, H. Cui, Q. Wei, R. Peng, L. Hong, J. Huang and Z. Ge, *Adv. Mater.* 2018, **30**, 1800075.

[16] G. Li, V. Shrotriya, J. Huang, Y. Yao, T. Moriarty, K. Emery and Y. Yang, *Nat. Mater.* 2005, **4**, 864-868.

[17] Y. Liang, Z. Xu, J. Xia, S. T. Tsai, Y. Wu, G. Li, C. Ray and L. Yu, *Adv. Mater.* 2010, **22**, 135-138.

[18] Y. Li, G. Xu, C. Cui and Y. Li, *Adv. Energy Mater.* 2018, **8**, 1701791.

[19] L. Tan, Y. Wang, J. Zhang, S. Xiao, H. Zhou, Y. Li, Y. Chen and Y. Li, *Adv. Sci.* 2019, **6**, 1801180.

[20] F. Qin, W. Wang, L. Sun, X. Jiang, L. Hu, S. Xiong, T. Liu, X. Dong, J. Li, Y. Jiang, J. Hou, K. Fukuda, T. Someya and Y. Zhou, *Nat. Commun.* 2020, **11**, 4508.

[21] L. Zhan, S. Li, T.-K. Lau, Y. Cui, X. Lu, M. Shi, C.-Z. Li, H. Li, J. Hou and H. Chen, *Energy Environ. Sci.* 2020, **13**, 635-645.

[22] Y. Cui, H. Yao, J. Zhang, T. Zhang, Y. Wang, L. Hong, K. Xian, B. Xu, S. Zhang, J. Peng, Z. Wei, F. Gao and J. Hou, *Nat. Commun.* 2019, **10**, 2515.

[23] J. Yuan, Y. Zhang, L. Zhou, C. Zhang, T. K. Lau, G. Zhang, X. Lu, H. L. Yip, S. K. So, S.

Beaupre, M. Mainville, P. A. Johnson, M. Leclerc, H. Chen, H. Peng, Y. Li and Y. Zou, *Adv. Mater.* 2019, **31**, 1807577.

[24] L. Hong, H. Yao, Z. Wu, Y. Cui, T. Zhang, Y. Xu, R. Yu, Q. Liao, B. Gao, K. Xian, H. Y. Woo, Z. Ge and J. Hou, *Adv. Mater.* 2019, **31**, 1903441.

[25] K. Jiang, Q. Wei, J. Y. L. Lai, Z. Peng, H. K. Kim, J. Yuan, L. Ye, H. Ade, Y. Zou and H. Yan, *Joule* 2019, **3**, 3020-3033.

[26] J. Yuan, T. Huang, P. Cheng, Y. Zou, H. Zhang, J. L. Yang, S. Y. Chang, Z. Zhang, W. Huang, R. Wang, D. Meng, F. Gao and Y. Yang, *Nat. Commun.* 2019, **10**, 570.

[27] S. Liu, J. Yuan, W. Deng, M. Luo, Y. Xie, Q. Liang, Y. Zou, Z. He, H. Wu and Y. Cao, *Nat. Photonics* 2020, **14**, 300–305.

[28] L. Qin, X. Liu, X. Zhang, J. Yu, L. Yang, F. Zhao, M. Huang, K. Wang, X. Wu, Y. Li, H. Chen, K. Wang, J. Xia, X. Lu, F. Gao, Y. Yi and H. Huang, *Angew. Chem. Int. Ed.* 2020, **59**, 2-9.

[29] C. Sun, S. Qin, R. Wang, S. Chen, F. Pan, B. Qiu, Z. Shang, L. Meng, C. Zhang, M. Xiao, C. Yang and Y. Li, *J. Am. Chem. Soc.* 2020, **142**, 1465-1474.

[30] G. Li, W.-H. Chang and Y. Yang, *Nat. Rev. Mater.* 2017, **2**, 17043.

[31] B. J. Worfolk, S. C. Andrews, S. Park, J. Reinspach, N. Liu, M. F. Toney, S. C. Mannsfeld and Z. Bao, *PNAS* 2015, **112**, 14138-14143.

[32] W. Huang, Z. Jiang, K. Fukuda, X. Jiao, C. R. McNeill, T. Yokota and T. Someya, *Joule* 2020, **4**, 128-141.

[33] D. Koo, S. Jung, J. Seo, G. Jeong, Y. Choi, J. Lee, S. M. Lee, Y. Cho, M. Jeong, J. Lee, J. Oh, C. Yang and H. Park, *Joule* 2020, **4**, 1021-1034.

[34] X. Chen, G. Xu, G. Zeng, H. Gu, H. Chen, H. Xu, H. Yao, Y. Li, J. Hou and Y. Li, *Adv. Mater.* 2020, **32**, 1908478.

[35] T. Yan, W. Song, J. Huang, R. Peng, L. Huang and Z. Ge, *Adv. Mater.* 2019, **31**, 1902210.

[36] X. Fan, R. Wen, Y. Xia, J. Wang, X. Liu, H. Huang, Y. Li, W. Zhu, Y. Cheng, L. Ma, J.

Fang, H. Tsai and W. Nie, *Solar RRL* 2020, **4**, 1900543.

[37] L. Sun, W. Zeng, C. Xie, L. Hu, X. Dong, F. Qin, W. Wang, T. Liu, X. Jiang, Y. Jiang and Y. Zhou, *Adv Mater* 2020, **32**, 1907840.

[38] Y. Sun, M. Chang, L. Meng, X. Wan, H. Gao, Y. Zhang, K. Zhao, Z. Sun, C. Li, S. Liu, H. Wang, J. Liang and Y. Chen, *Nat. Electron.* 2019, **2**, 513-520.

[39] W. Zhang, W. Song, J. Huang, L. Huang, T. Yan, J. Ge, R. Peng and Z. Ge, *J. Mater. Chem. A* 2019, **7**, 22021-22028.

[40] M. S. White, M. Kaltenbrunner, E. D. Głowacki, K. Gutnichenko, G. Kettlgruber, I. Graz, S. Aazou, C. Ulbricht, D. A. M. Egbe, M. C. Miron, Z. Major, M. C. Scharber, T. Sekitani, T. Someya, S. Bauer and N. S. Sariciftci, *Nat. Photonics* 2013, **7**, 811-816.

[41] M. Kaltenbrunner, M. S. White, E. D. Glowacki, T. Sekitani, T. Someya, N. S. Sariciftci and S. Bauer, *Nat. Commun.* 2012, **3**, 770.

[42] T. Yokota, P. Zalar, M. Kaltenbrunner, H. Jinno, N. Matsuhisa, H. Kitanosako, Y. Tachibana, W. Yukita, M. Koizumi and T. Someya, *Sci. Adv.* 2016, **2**, 1501856.

[43] W. Song, B. Fanady, R. Peng, L. Hong, L. Wu, W. Zhang, T. Yan, T. Wu, S. Chen and Z. Ge, *Adv. Energy Mater.* 2020, **10**, 2000136.

[44] A. Ghanbari, M. C. Heuzey, P. J. Carreau and M. T. Ton-That, *Polymer* 2013, **54**, 1361-1369.

[45] H. Ghasemi, P. J. Carreau, M. R. Kamal and S. H. Tabatabaei, *Polym. Eng. Sci.* 2012, **52**, 420-430.

[46] Y. Wu, T. Zhang, Y. Zhang, G. Zhou, H. Zhang and X. Zhang, *Surf. Coat. Tech.* 2001, **148**, 221–225.

[47] B. S. Hardy, K. Uechi, J. Zhen and H. Pirouz Kavehpour, *Lab Chip* 2009, **9**, 935-8.

[48] L.-K. Ma, Y. Chen, P. C. Y. Chow, G. Zhang, J. Huang, C. Ma, J. Zhang, H. Yin, A. M. Hong Cheung, K. S. Wong, S. K. So and H. Yan, *Joule* 2020, **4**, 1486-1500.

[49] Y. Cui, L. Hong and J. Hou, *ACS Appl. Mater. Interfaces* 2020, **12**, 38815–38828.

[50] Y. Cui, H. Yao, T. Zhang, L. Hong, B. Gao, K. Xian, J. Qin and J. Hou, *Adv. Mater.* 2019, **31**, 1904512.

[51] Y. Cui, Y. Wang, J. Bergqvist, H. Yao, Y. Xu, B. Gao, C. Yang, S. Zhang, O. Inganäs, F. Gao and J. Hou, *Nat. Energy* 2019, **4**, 768-775.

[52] H. Yin, J. K. W. Ho, V. Piradi, S. Chen, X. Zhu and S. K. So, *Small Methods* 2020, **4**, 2000136.

[53] Y. Cho, T. Kumari, S. Jeong, S. M. Lee, M. Jeong, B. Lee, J. Oh, Y. Zhang, B. Huang, L. Chen and C. Yang, *Nano Energy* 2020, **75**, 104896.

[54] K. Li, Y. Zhang, H. Zhen, H. Wang, S. Liu, F. Yan and Z. Zheng, *J. Mater. Chem. A* 2017, **5**, 969-974.

[55] Z. Ren, J. Zhou, Y. Zhang, A. Ng, Q. Shen, S. H. Cheung, H. Shen, K. Li, Z. Zheng, S. K. So, A. B. Djurišić and C. Surya, *Sol. Energy Mater. Sol. Cells* 2018, **179**, 36-44.

[56] B.-K. Chao, H.-H. Cheng, L.-W. Nien, M.-J. Chen, T. Nagao, J.-H. Li and C.-H. Hsueh, *Appl. Surf. Sci.* 2015, **357**, 615-621.

[57] C. Trompoukis, O. El Daif, V. Depauw, I. Gordon and J. Poortmans, *Appl. Phys. Lett.* 2012, **101**, 103901.

[58] C. Trompoukis, I. Abdo, R. Cariou, I. Cosme, W. Chen, O. Deparis, A. Dmitriev, E. Drouard, M. Foldyna, E. G. Caurel, I. Gordon, B. Heidari, A. Herman, L. Lalouat, K.-D. Lee, J. Liu, K. Lodewijks, F. Mandorlo, I. Massiot, A. Mayer, V. Mijkovic, J. Muller, R. Orobtchouk, G. Poulain, P. Prod'Homme, P. R. i. Cabarrocas, C. Seassal, J. Poortmans, R. Mertens, O. E. Daif and V. Depauw, *Phys. Status Solidi* 2015, **212**, 140-155.

[59] A. A. Tseng, A. Notargiacomo and T. P. Chen, *J. Vac. Sci. Technol.* 2005, **23**, 877.

[60] R. Peng, W. Song, T. Yan, B. Fanady, Y. Li, Q. Zhan and Z. Ge, *J. Mater. Chem. A* 2019, **7**, 11460-11467.

[61] A. Höpe, *Spectrophotometry - Accurate Measurement of Optical Properties of Materials* 2014, 179-219.

[62] D. G. Stavenga, S. Foletti, G. Palasantzas and K. Arikawa, *Proc. Biol. Sci.* 2006, **273**, 661-7.

[63] S. K. Saini and R. V. Nair, *J. Appl. Phys.* 2019, **125**, 103102.

[64] B. Dudem, I. S. Jin, A. R. Mule, J. W. Jung and J. S. Yu, *ACS Sustain. Chem. Eng.* 2019, **7**, 12981-12989.

[65] A. Ali, S. Ali, H. Ali, K. Alam, W. Ali, N. Khan, S. Manzoor, Z. Holman and M. Arif, *Key Eng. Mater.* 2018, **778**, 283-289.

[66] Z. Fang, H. Zhu, W. Bao, C. Preston, Z. Liu, J. Dai, Y. Li and L. Hu, *Energy Environ. Sci.* 2014, **7**, 3313-3319.

[67] A. Marmur, *Langmuir* 2008, **24**, 7573-7579.

[68] M. Vosgueritchian, D. J. Lipomi and Z. Bao, *Adv. Funct. Mater.* 2012, **22**, 421-428.

[69] S. Xiong, L. Hu, L. Hu, L. Sun, F. Qin, X. Liu, M. Fahlman and Y. Zhou, *Adv. Mater.* 2019, **31**, 1806616.

[70] H. Cui, W. Song, B. Fanady, R. Peng, J. Zhang, J. Huang and Z. Ge, *Sci. China Chem.* 2019, **62**, 500-505.

[71] I. Hwang, Y. Jeong, Y. Shiratori, J. Park, S. Miyajima, I. Yoon and K. Seo, *Cell Rep. Phys. Sci.* 2020, **1**, 100242.

[72] I. Hwang, D. Choi, S. Lee, J. H. Seo, K. H. Kim, I. Yoon and K. Seo, *ACS. Appl. Mater. Interfaces* 2017, **9**, 21276-21282.

[73] J. Ma, Y. Ai, L. Kang, W. Liu, Z. Ma, P. Song, Y. Zhao, F. Yang and X. Wang, *Nanoscale Res. Lett.* 2018, **13**, 332.

[74] J. D. Myers, W. Cao, V. Cassidy, S.-H. Eom, R. Zhou, L. Yang, W. You and J. Xue, *Energy Environ. Sci.* 2012, **5**, 6900.

[75] J. Qin, L. Lan, S. Chen, F. Huang, H. Shi, W. Chen, H. Xia, K. Sun and C. Yang, *Adv. Funct. Mater.* 2020, 2002529.

[76] X. Meng, Z. Xing, X. Hu, Z. Huang, T. Hu, L. Tan, F. Li and Y. Chen, *Angew. Chem. Int.*

Ed. 2020, **59**, 16602–16608.

[77] X. Hu, Z. Huang, F. Li, M. Su, Z. Huang, Z. Zhao, Z. Cai, X. Yang, X. Meng, P. Li, Y. Wang, M. Li, Y. Chen and Y. Song, *Energy Environ. Sci.* 2019, **12**, 979-987.

[78] D. J. Lipomi, B. C. Tee, M. Vosgueritchian and Z. Bao, *Adv. Mater.* 2011, **23**, 1771-5.

[79] S. Kim, M. Jahandar, J. H. Jeong and D. C. Lim, *Curr. Altern. Energy* 2019, **3**, 3-17.

[80] Y. Cao, Y. Liu, S. M. Zakeeruddin, A. Hagfeldt and M. Grätzel, *Joule* 2018, **2**, 1108-1117.

[81] M. A. Saeed, S. H. Kim, S. Y. Lee and J. W. Shim, *Thin Solid Films* 2020, **704**, 138006.

[82] M. A. Green, *Solid-State Electron* 1981, **24**, 788-789.

[83] M. Benghanem, *Appl. Energy* 2011, **88**, 1427-1433.

[84] H. S. S. Pour, H. K. Beheshti and M. Rahnama, *Energy Source Part A* 2011, **33**, 1281-1290.

[85] J. L. Balenzategui and F. Chenlo, *Sol. Energy Mater. Sol. Cells* 2005, **86**, 53-83.

[86] N. Reiners, U. Blieske and S. Siebentritt, *IEEE J. Photovolt.* 2018, **8**, 1738-1747.

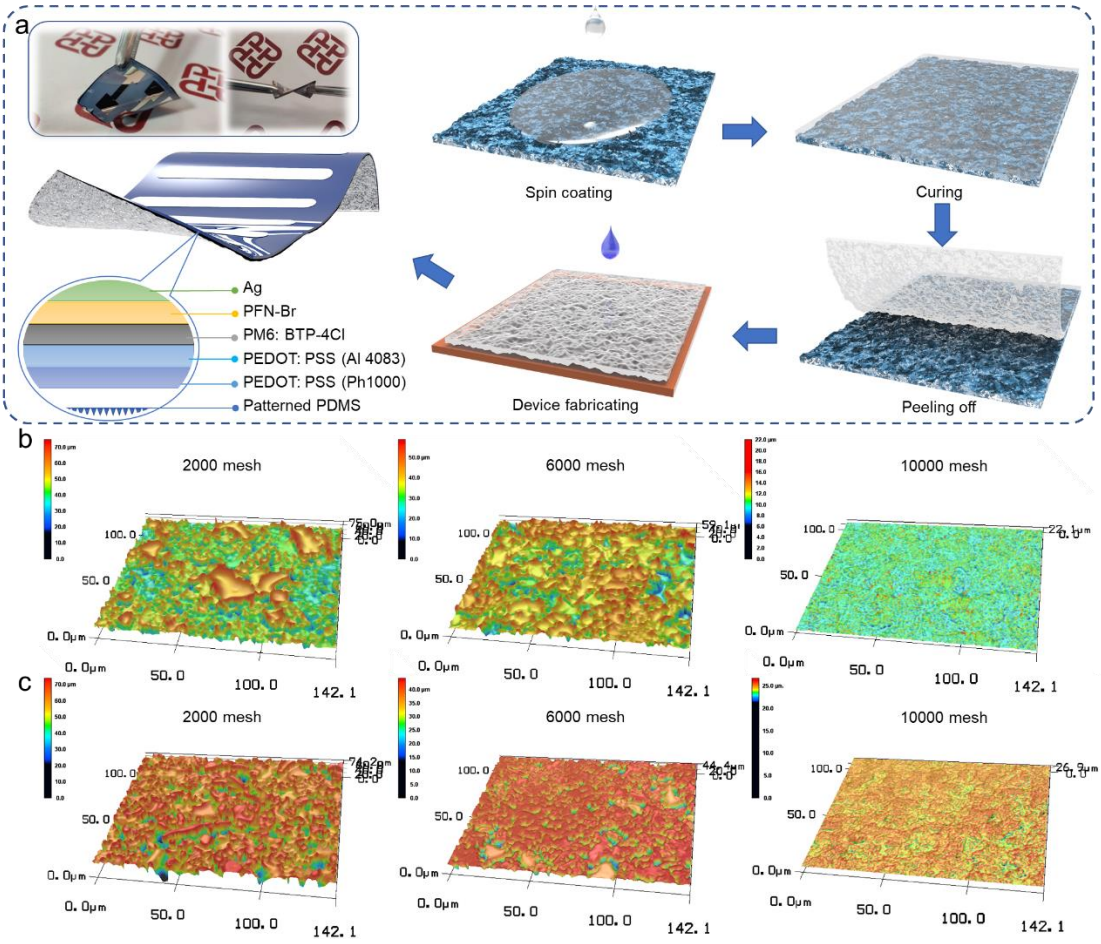

Figure 1 (a) Schematic diagram for surface-textured PDMS substrate fabrication and corresponding device structure; 3D surface image of abrasive paper (b) and duplicated PDMS (c) with different mesh numbers.

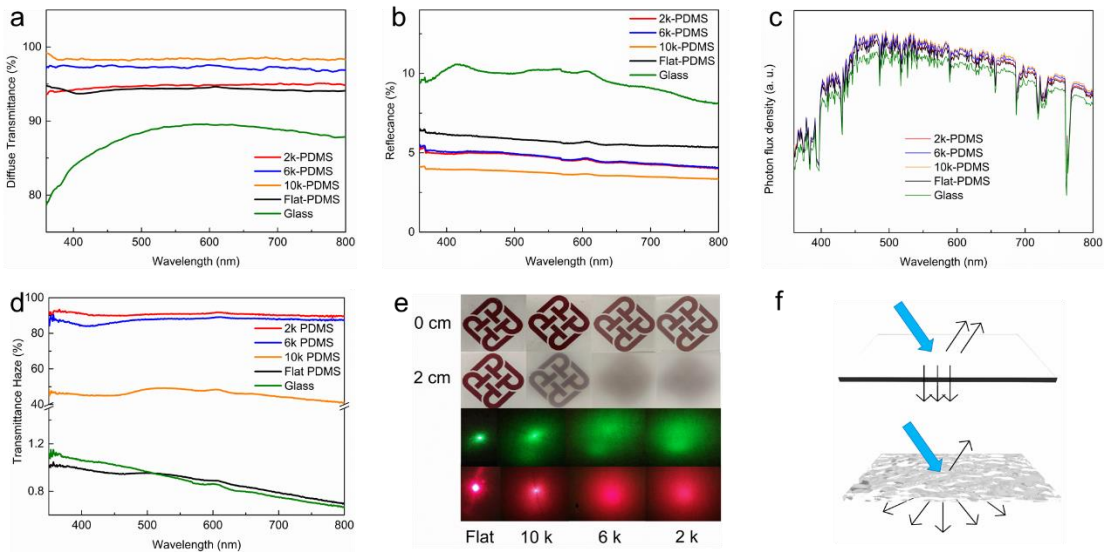

Figure 2 (a) Diffuse transmittance spectra; (b) Reflection spectra; (c) Photon flux density; (d) Transmittance haze of glass and PDMS substrates with different mesh number; (e) Haze effect of patterned PDMS substrates; (f) Schematic diagram of light scattering effect of patterned PDMS substrates

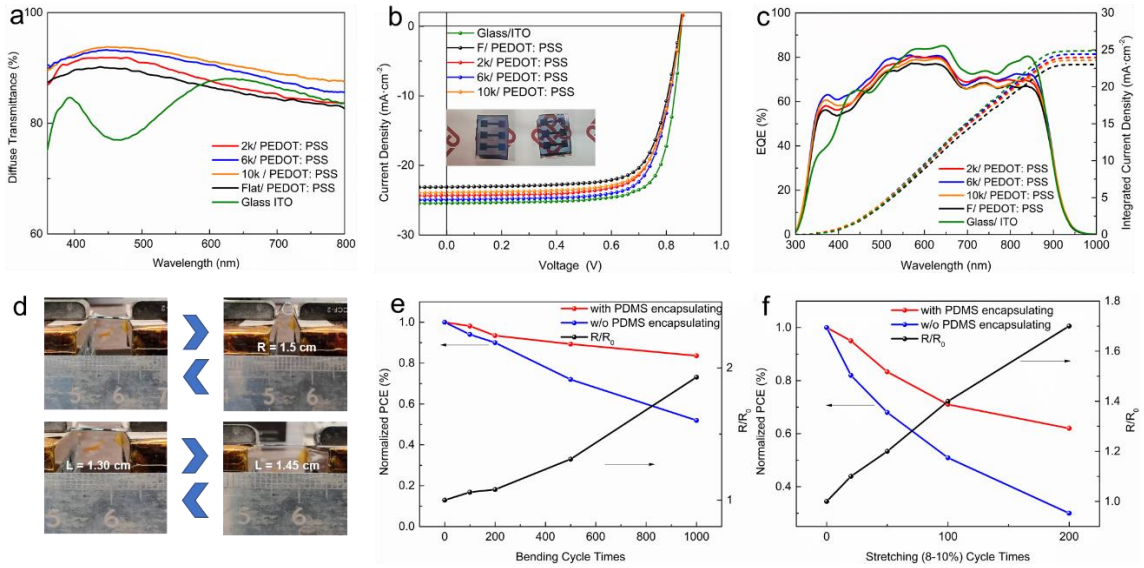

Figure 3 (a) Diffuse transmittance of glass/ITO and PDMS/PEDOT: PSS electrodes; (b) J-V curves; (c) EQE spectra of devices; (d) The schematic diagram of (Upper) bending with a radius of 1.5 cm, (lower) stretch ration of 8-10%; PCE decrease and sheet resistance increase with (e) bending and (f) stretching (8-10%) of flexible devices.

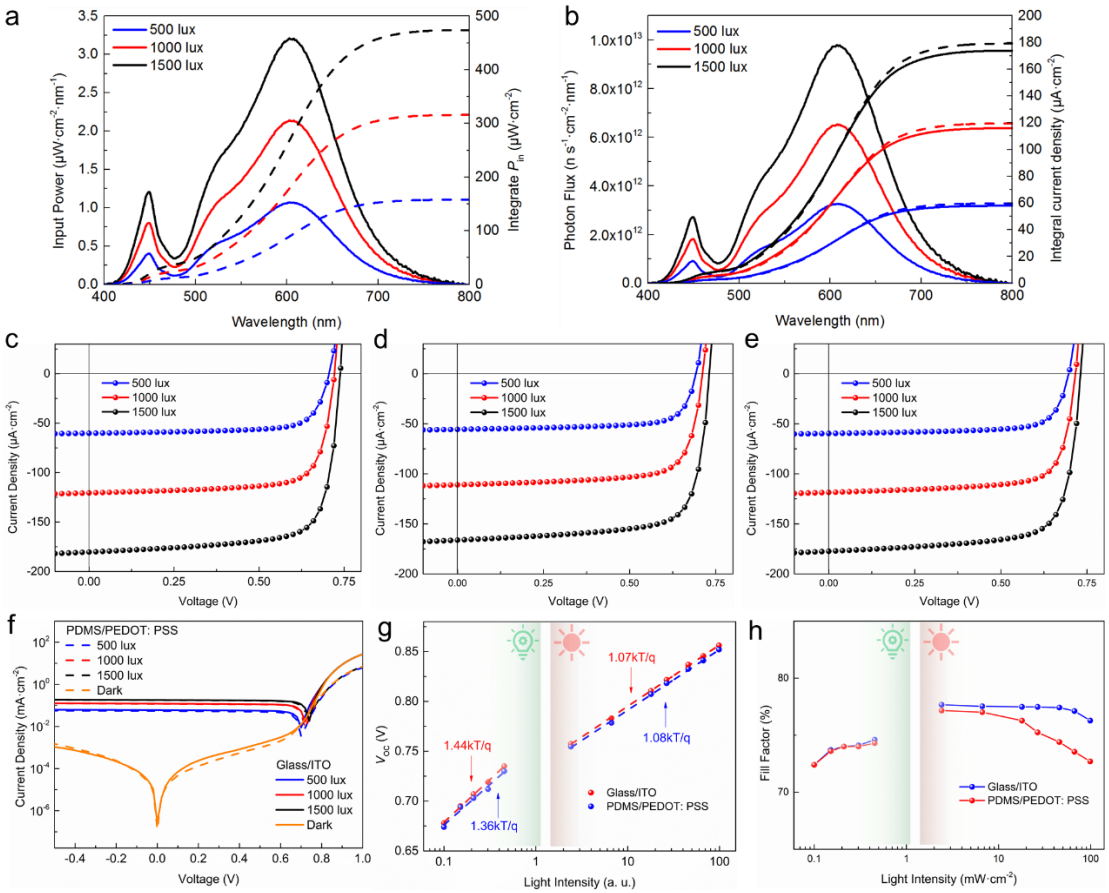

Figure 4 (a) Input power and integrated power spectra of warm 2700 K LED at 500, 1000, 1500 lux; (b) Photon flux and integrated current density spectra over the warm white 2,700 K LED at 500, 1000, 1500 lux: Glass/ITO (Solid line) and 6k-PDMS/PEDOT: PSS (Dash line); *J-V* curves devices warm white 2,700 K LED at 500, 1000, 1500 lux under based on (c) Glass/ITO; (d) F-PDMS/PEDOT: PSS and (e) 6k-PDMS/PEDOT: PSS; (f) The current density (log scale) as a function of the voltage for rigid and flexible devices under dark and LED illumination; (g) V_{OC} and (h) FF versus light intensity: 1-100 mW·cm^{-2} under solar simulator and 0.1 to 1 mW·cm^{-2} under warm LED 2700 K

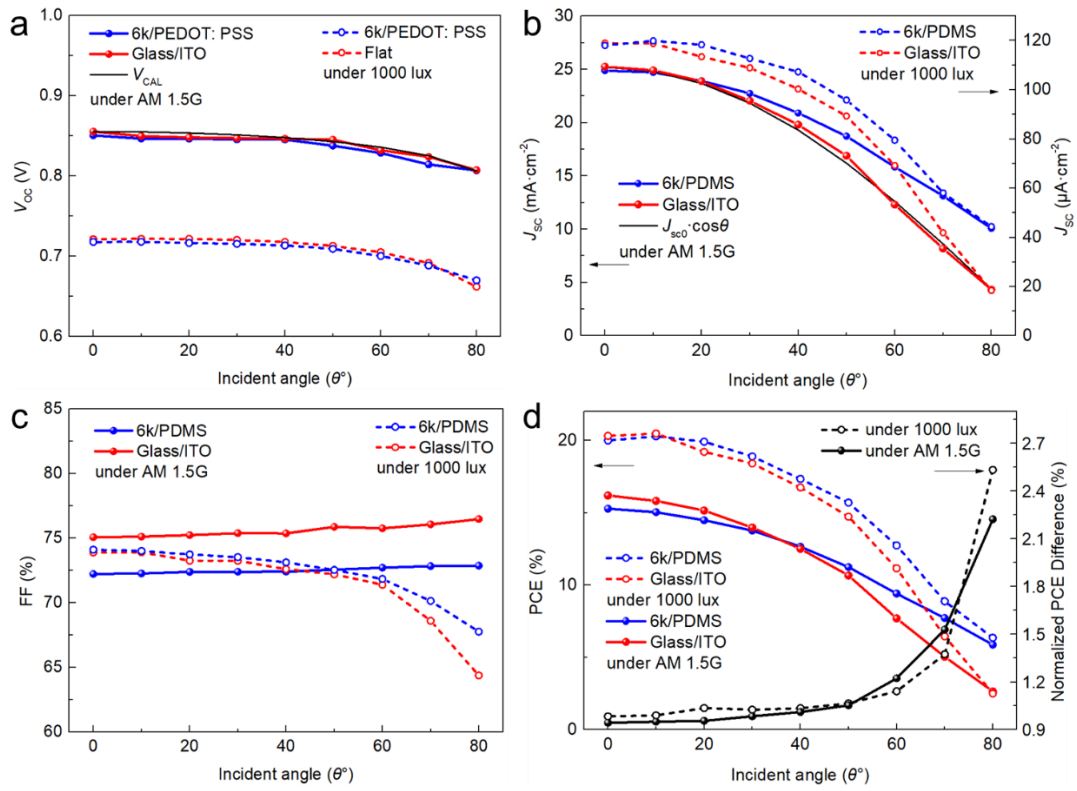

Figure 5 Incident angular dependent of (a) V_{OC}, (b) J_{SC}, (c) FF and (d) PCE/PCE enhancement of devices based on glass/ITO and 6k-PEDOT: PSS under AM 1.5G and 1000 lux of LED 2700K

Table 1 Photovoltaic parameters of OPV cells based on different substrates and electrodes under AM 1.5G, 100 mW·cm^{-2}

Devices	V_{OC} [V]	J_{SC} [mA·cm^{-2}]	J_{Cal} [mA·cm^{-2}]	FF [%]	PCE (ave*) [%]	R_{series} [Ω cm^2]	R_{shunt} [kΩ cm^2]
Glass/ITO	0.860	25.4	24.8	75.1	16.3 (16.0)	2.21	2.00
F PDMS/PEDOT: PSS	0.852	23.3	23.0	72.6	14.2 (14.0)	4.14	1.92
2k-PDMS/PEDOT: PSS	0.853	24.3	23.9	71.9	14.9 (14.6)	3.74	1.62
6k-PDMS/PEDOT: PSS	0.853	25.0	24.4	72.1	15.3 (14.8)	3.32	2.06
10k-PDMS/PEDOT: PSS	0.852	24.0	23.6	72.3	14.7 (14.5)	3.54	1.81

*: average data were collected from over 20 devices.

Table 2 Photovoltaic parameters of OPV cells based on different substrates and electrodes under 2700K LED lamp

Devices	Intensity [lux]	P_{in} [$\mu W \cdot cm^{-2}$]	V_{OC} [V]	J_{SC} [$\mu A \cdot cm^{-2}$]	J_{Cal} [$\mu A \cdot cm^{-2}$]	FF [%]	P_{out} [$\mu W \cdot cm^{-2}$]	PCE (ave*) [%]
Glass/ITO	500	158.0	0.702	60.2	59.0	73.7	31.1	19.7 (19.5)
	1000	315.9	0.723	119.8	118.1	74.1	64.2	20.3 (19.7)
	1500	473.9	0.738	179.2	177.1	74.4	98.4	20.8 (20.5)
F PDMS/ PEDOT: PSS	500	158.0	0.694	55.6	55.1	73.2	28.2	17.9 (17.7)
	1000	315.9	0.712	110.9	110.3	73.8	58.3	18.4 (18.0)
	1500	473.9	0.730	166.2	165.4	74.2	90.0	19.0 (18.5)
6k-PDMS/ PEDOT: PSS	500	158.0	0.697	59.7	58.6	73.6	30.5	19.3 (19.0)
	1000	315.9	0.715	118.6	117.2	74.0	62.8	19.9 (19.4)
	1500	473.9	0.732	178.4	175.8	74.3	97.0	20.5 (20.0)

*Jiaming Huang[1, 2], Zhiwei Ren[1], Yaokang Zhang[3], Kuan Liu[1], Hengkai Zhang[1,2], Hua Tang[1], Cenqi Yan[1], Zijian Zheng[3] and Gang Li[1, 2,]**

Stretchable ITO-free Organic Solar Cells with Intrinsic Anti-reflection Substrate for High-efficiency Outdoor and Indoor Energy Harvesting

This work reports a simple, generic and effective approach towards high-performance, stretchable outdoor and indoor organic photovoltaic, and achieves a high PCE of 15.3% under 1-sun illumination. Under the indoor illumination, the stretchable device shows a comparable performance (20.5% vs 20.8%) to glass/ITO-based devices. The stretchable device shows 1.5−2 times PCE larger than rigid device at large incident angle.

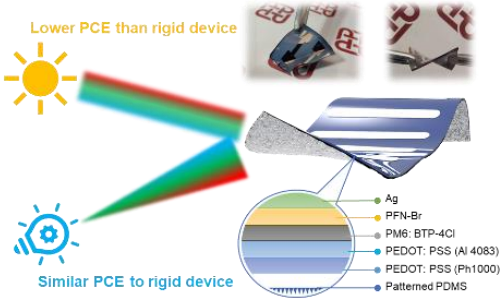

Supporting Information

Stretchable ITO-free Organic Solar Cells with Intrinsic Anti-reflection Substrate for High-efficiency Outdoor and Indoor Energy Harvesting

Jiaming Huang[1, 2], Zhiwei Ren[1], Yaokang Zhang[3], Kuan Liu[1], Hengkai Zhang[1,2], Hua Tang[1], Cenqi Yan[1], Zijian Zheng[3] and Gang Li[1, 2,] *

J. Huang, Dr. Z. Ren, Dr. K. Liu, H. Zhang, H. Tang, Dr. C. Yan, and Prof. G. Li
Department of Electronic and Information Engineering, Research Institute for Smart Energy (RISE), The Hong Kong Polytechnic University, Hung Hom, Kowloon, Hong Kong, China.

J. Huang, H. Zhang, and Prof. G. Li
The Hong Kong Polytechnic University Shenzhen Research Institute, Shenzhen 518057, China.

Dr. Y. Zhang, Prof. Z. Zheng
Laboratory for Advanced Interfacial Materials and Devices, Institute of Textiles and Clothing, The Hong Kong Polytechnic University, Hung Hom, Kowloon, Hong Kong, China.

Correspondent authors: G. L. (e-mail: gang.w.li@polyu.edu.hk)

1. Materials

PEDOT: PSS (PH1000) and PEDOT: PSS (Al4083) were purchased from Heraeus Clevis. PM6, BTP-4Cl, PFN-Br were purchased from Solarmer Materials (Beijing) Inc and were used without any further purification. Other chemicals were purchased from Sigma-Aldrich, Inc. The full mane of materials mentioned in the paper is the following. ITO glass was purchased from Zhuhai Kaivo Optoelectronic Technology Co., Ltd. PDMS precursor and curing agent were purchased from Dow Corning.

PM6: Poly[(2,6-(4,8-bis(5-(2-ethylhexyl-3-fluoro) thiophen-2-yl)-benzo[1,2-b:4,5-']dithiophene)) -alt-(5,5-(1',3'-di-2-thienyl-5',7'-bis(2- ethylhexyl) benzo[1',2'-c:4',5'-c']dithiophene-4,8-dione)]

BTP-4Cl: 2,2'-((2Z,2'Z)-((12,13-bis(2-ethylhexyl)-3,9-diundecyl-12,13-dihydro-[1,2,5]thiadiazolo [3,4-e]thieno [2",3'':4',5'] thieno[2',3':4,5]pyrrolo[3,2-g]thieno[2',3':4,5]thieno[3,2-b]indole-2,10-diyl)bis (methanylylidene)) bis(5,6-dichloro-3-oxo-2,3-dihydro-1H-indene-2,1-diylidene)) dimalononitrile

PFN-Br: Poly(9,9-bis(3'-(N,N-dimethyl)-N-ethylammoinium-propyl-2,7-fluorene)-alt-2,7-(9,9-dioctylfluorene))dibromide

2. Characterization and Measurement

The surface morphology of abrasive paper and PDMS were investigated by a 3D Laser scanning microscope (KEYENCE VK-X200) and SEM (Tescan VEGA3). The optical property was measured by Varian Cary® 300 UV-Vis spectrophotometers, Agilent Technologies, with an integrating sphere. The sheet resistance was conducted by four-terminal measurement. AFM height images and phase images were obtained using a Bruker Multimode 8 scanning probe microscope (tapping mode). The contact angle was measured by the optical contact angle measurement (SDC-350, Guangdong Dynetech). The PEDOT: PSS electrodes were characterized by ultraviolet photoemission spectroscopy (Kratos AXIS ULTRA HAS, He−Iα = 21.22 eV) and XPS (Kratos AXIS ULTRA HAS, monochromated Al Kα = 1486.6 eV). The *J-V* curves were measured in the glovebox with a Keithley 2400 measure unit under 1 sun, AM 1.5G spectra (100 $mW \cdot cm^{-2}$) from a solar simulator (Enli Tech. Co., Ltd., Taiwan). The light intensity was calibrated with a 20 mm×20 mm monocrystalline silicon reference cell with KG5 filter (Enli Tech. Co., Ltd., Taiwan). The EQE od devices were measured by QE-R3-011 (Enli Tech. Co., Ltd., Taiwan). The light intensity at each wavelength was calibrated with a standard single-crystal Si photovoltaic cell. LED lamp was purchased from Philips (CorePro E27 LED GLS Bulb 8 W(60W), 2700K, Warm White, GLS shape). The light intensity and spectra were measured by Ocean Optics spectrometer (QE65000).

3. Devices Fabricating

The PDMS precursor and curing reagents were mixed at a ratio of 10:1 (w/w), degassed, and spin coating onto the abrasive paper with 800 rpm for 1 min. It is found that PDMS would be dyed by some abrasive papers after curing at 70 ℃ for 2 h. To avoid it, the PDMS was cured at room temperature for about 2 days to prepare cross-linked PDMS substrate. The cured PDMS was peeled off from abrasive paper and laminate onto a glass for further use. The obtained PDMS substrate was treated with UVO for 20 min. The PH1000 doped with Capstone™ FS-3100 was spin-coated at 1600 rpm for 40 s, followed by thermal annealing at 100 ℃ for 10 min. Acetic acid (99%) was then dropped onto the obtained pristine PH1000 film for acid treatment for 10 min. Then the films were annealed at 80 for 15 min to remove the residue acid. Glass/ITO was washed by DI water, acetone, and isopropanol for 30 min. The Al 4083 was then spin-coated onto the glass/ITO and PDMS/PH1000 at 3500 rpm for 40 s, followed by thermal annealing at 100 ℃ for 10 min. For the active layer, 20 $mg \cdot mL^{-1}$ PM6 and BTP-4Cl (1:1) was solved in chlorobenzene and stirred at 80 ℃ overnight. Then the solution was spin-coated at 2200 rpm for 40 s and annealing at 100 ℃ for 10 min. PFN-Br (0.5 $mg \cdot mL^{-1}$ in methanol) was spin-coated at 3000 rpm for 40 s. Finally, the Ag electrode was deposited thermal evaporation to complete the whole device. To protect the Ag electrode, the mix PDMS was bladed onto the device and curing at r. t. for 24 h in glovebox.

4. Illuminance calculation

The value of illuminance was calculated from the equation:

$$E_V = K_m \int_0^\infty E_\lambda \cdot V_\lambda \cdot d\lambda$$

Where Km is 683lm/W, E_λ is the input power spectra, V_λ is the Luminosity function

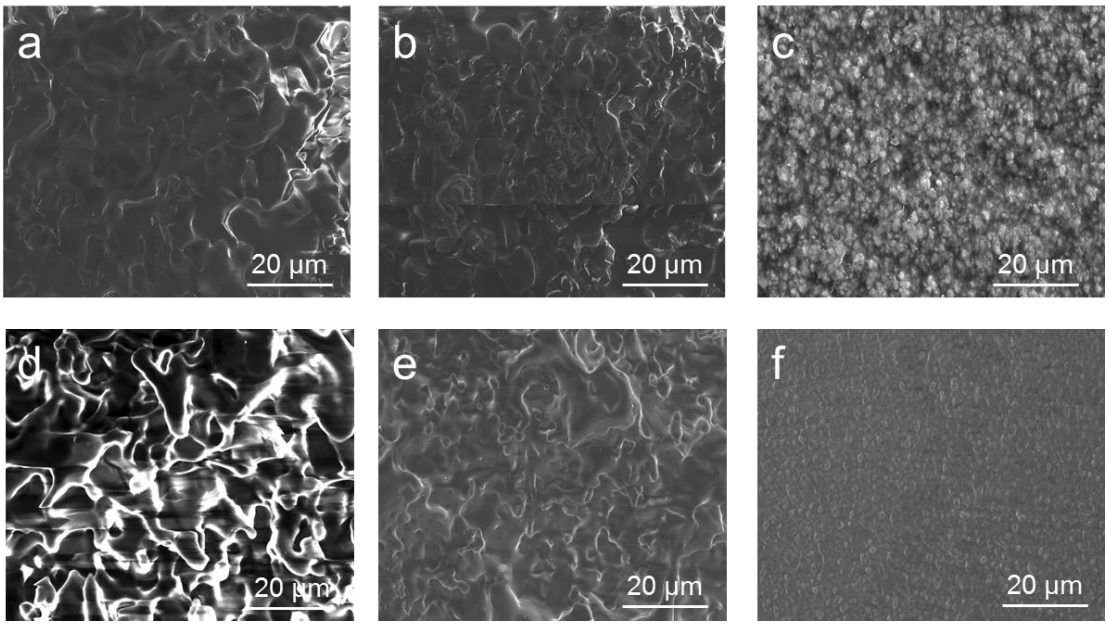

Figure S1 SEM images of abrasive paper (a-c) and duplicated PDMS (d-f) with different mesh number: a, d) 2k mesh; b, e) 6k mesh; c, f) 10k mesh

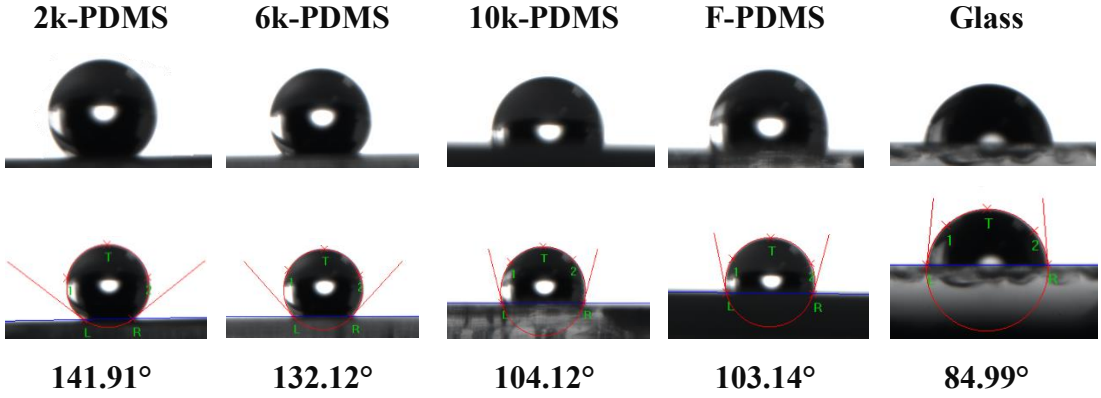

Figure S2 Contact angle of the water droplet on the patterned side surface of PDMS and glass

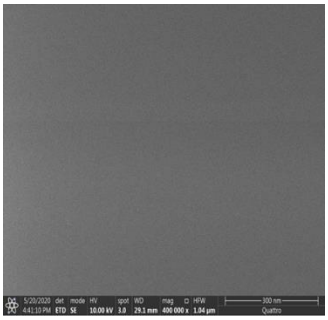

Figure S3 SEM image of PDMS substrate after acetic acid treatment

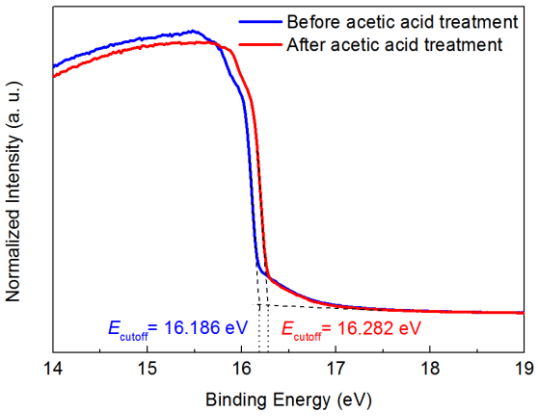

Figure S4 UPS spectra of pristine and acid treated PDMS/PEDOT: PSS electrodes

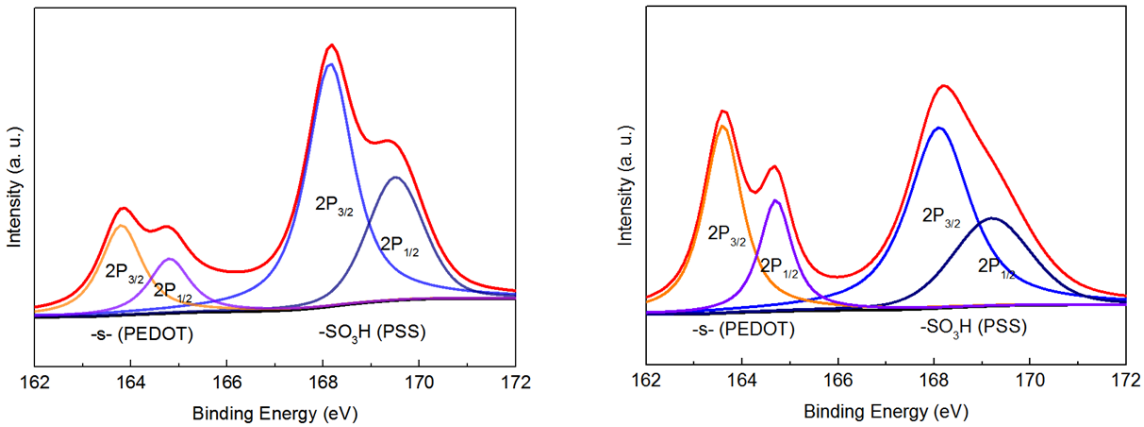

Figure S5 XPS spectra of pristine (left) and acetic acid treated (right) PDMS/PEDOT: PSS electrodes

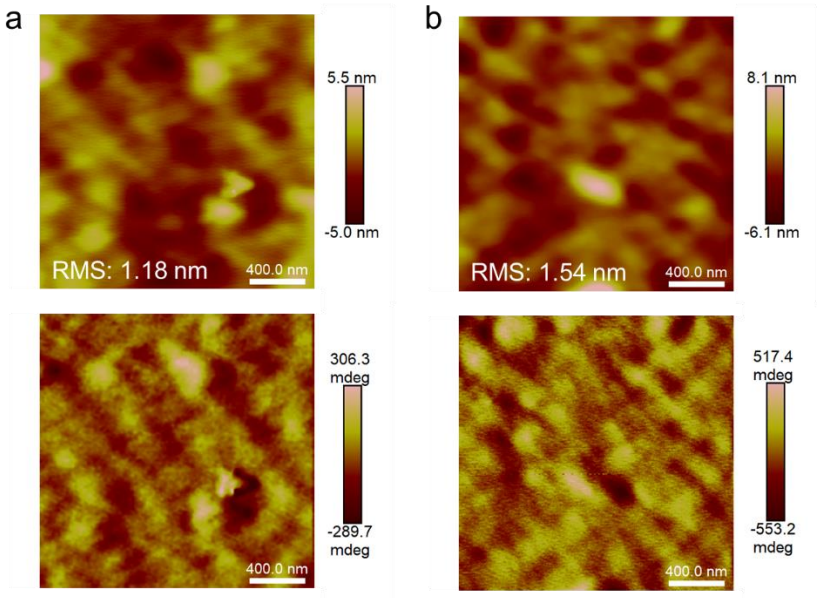

Figure S6 AFM morphology images of pristine (a); acetic acid treatment (b) PEDOT: PSS electrodes based on PDMS substrates; Height images (upper) and phase images (lower)

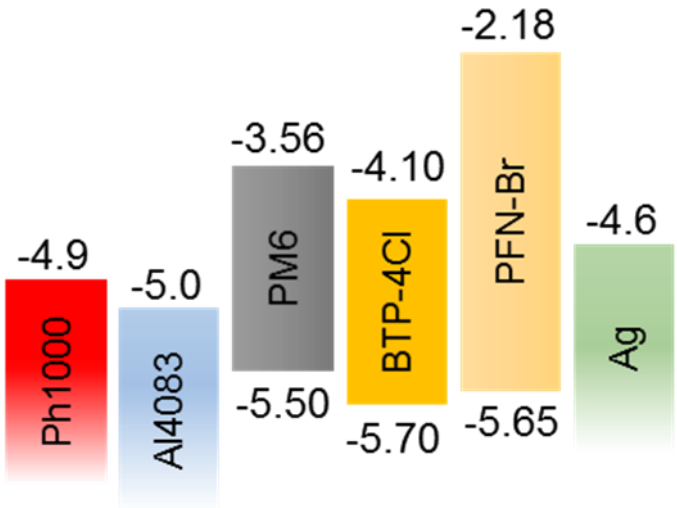

Figure S7 Energy level diagram of OPV device

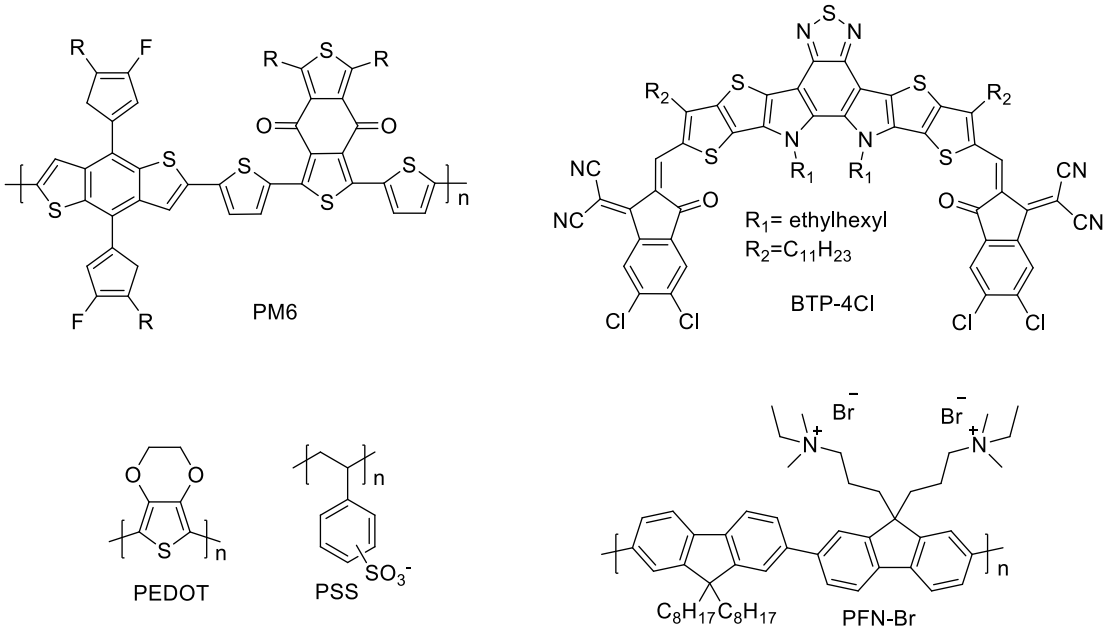

Figure S8 Chemical structures of materials in this work

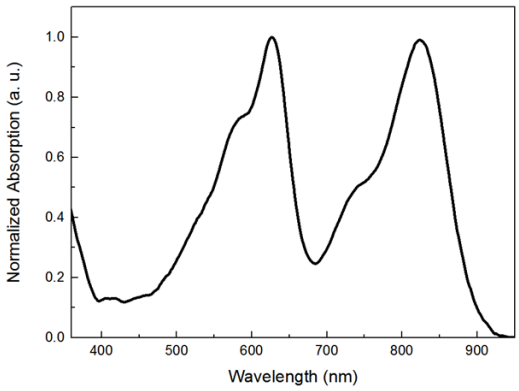

Figure S9 Normalized absorption of active layer based on PM6: BTP-4Cl

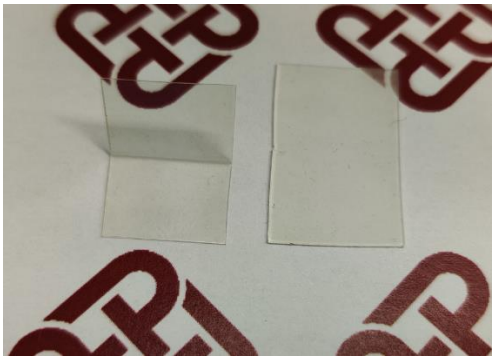

Figure S10 The images of substrates after completely folding (left: PET; right: PDMS)

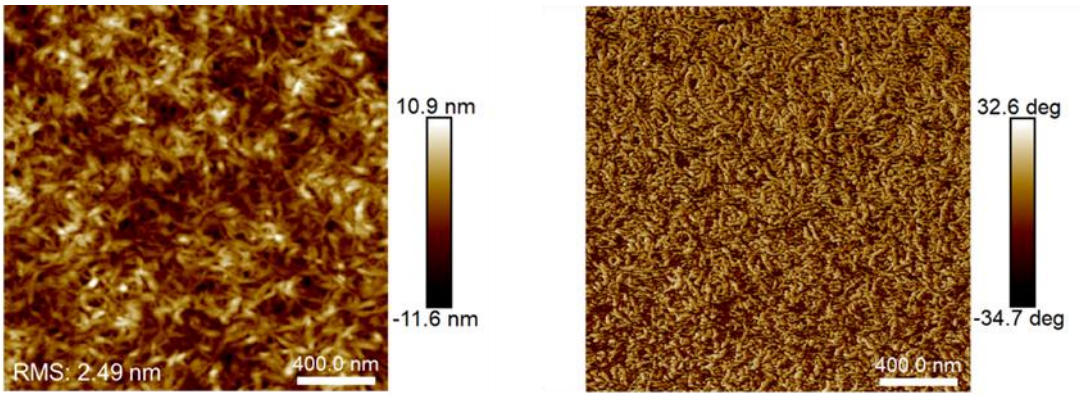

Figure S11 AFM images of active layer (PM6: BTP-4Cl) based on PDMS/PEDOT: PSS (PH1000)/PEDOT: PSS (Al4083); Height image (left) and phase image (right)

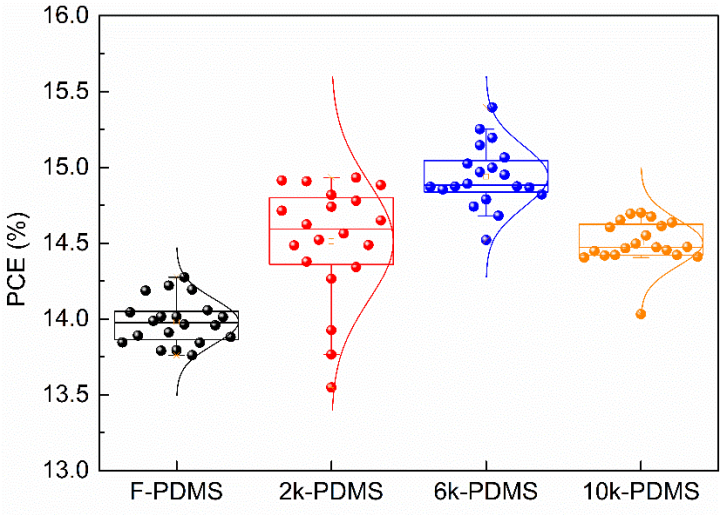

Figure S12 The box plot of photovoltaic performance of flexible devices based on anti-reflection substrates

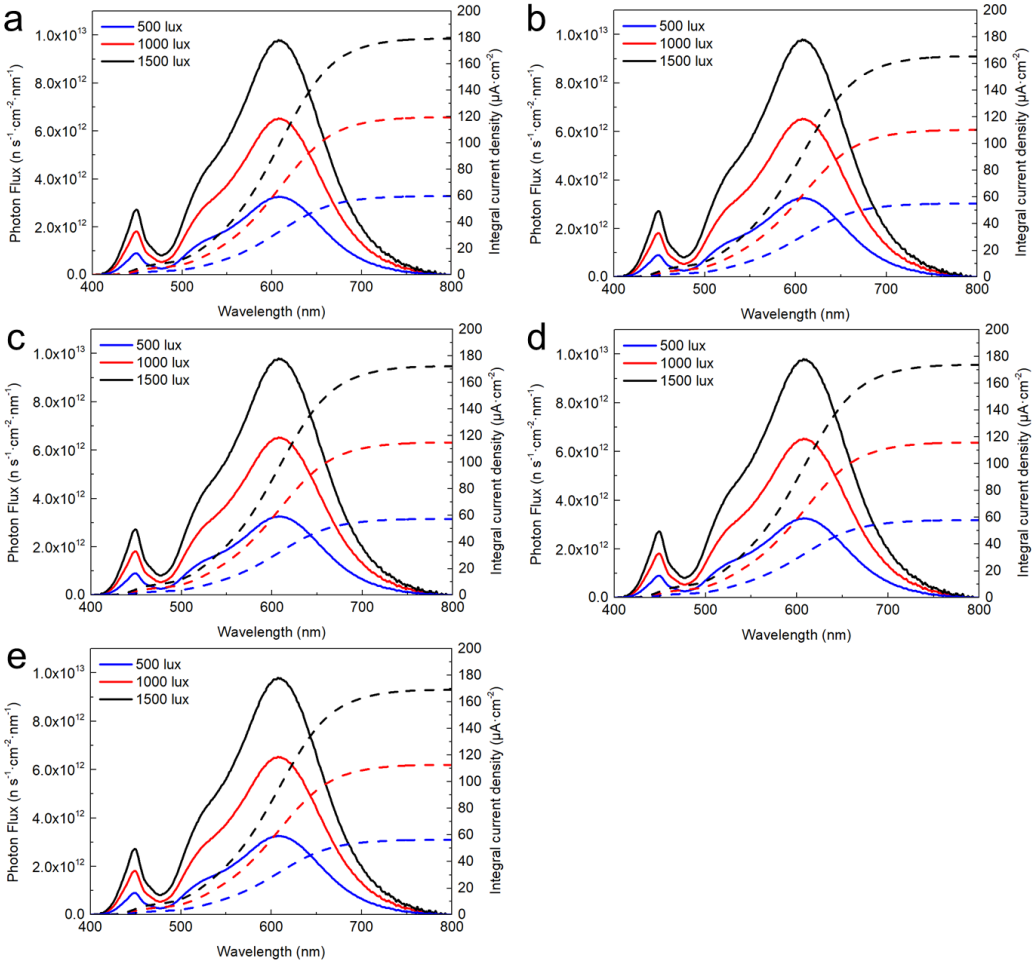

Figure S13 Photon flux spectra and corresponding integral current density of a) Glass/ITO; b) F-PDMS/PEDOT: PSS; c) 2k-PDMS/PEDOT: PSS; d) 6k-PDMS/PEDOT: PSS; e) 10k-PDMS/PEDOT: PSS based device

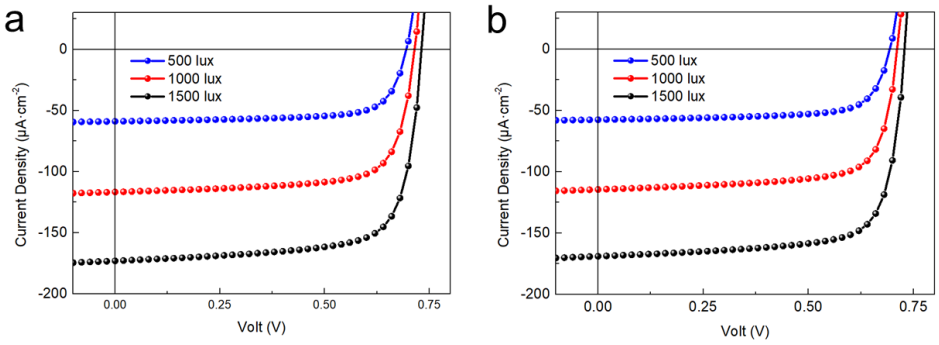

Figure S14 *J-V* curves of a) 2k-PDMS/PEDOT: PSS; b) 10k-PDMS/PEDOT: PSS based device

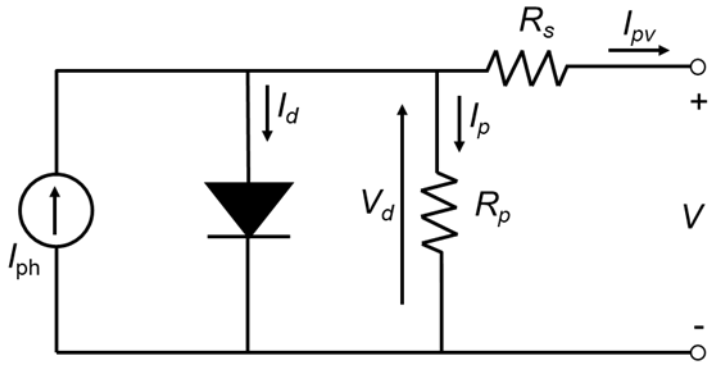

Figure S15 The equivalent circuit model of solar cells

Table S1 Improvement of rigid OPV devices performance after laminating the anti-reflection films onto glass substrates

Devices	V_{OC} [V]	J_{SC} [mA·cm^{-2}]	FF [%]	PCE [%]
Glass/ITO	0.857	25.2	75.7	16.3
F PDMS/glass/ITO	0.857	25.5	75.5	16.5
2k-PDMS/glass/ITO	0.858	25.7	75.2	16.6
6k-PDMS/glass/ITO	0.858	26.2	75.0	16.9
10k-PDMS/glass/ITO	0.858	25.8	75.2	16.6

Table S2 Photovoltaic parameters of OPV cells based on different substrates and electrodes under 2700K LED lamp

Devices	Intensity [lux]	P_{in} [μW·cm^{-2}]	V_{OC} [V]	J_{SC} [μA·cm^{-2}]	J_{CAL} [μA·cm^{-2}]	FF [%]	P_{out} [μW·cm^{-2}]	PCE (ave*) [%]
Glass/ITO	500	158.0	0.702	60.2	59.0	73.7	31.1	19.7 (19.5)
	1000	315.9	0.723	119.8	118.1	74.1	64.2	20.3 (19.7)
	1500	473.9	0.738	179.2	177.1	74.4	98.4	20.8 (20.5)
F-PDMS/ PEDOT: PSS	500	158.0	0.694	55.6	55.1	73.2	28.2	17.9 (17.7)
	1000	315.9	0.712	110.9	110.3	73.8	58.3	18.4 (18.0)
	1500	473.9	0.730	166.2	165.4	74.2	90.0	19.0 (18.5)
2k-PDMS/ PEDOT: PSS	500	158.0	0.695	58.9	57.4	73.1	29.9	18.9 (18.6)
	1000	315.9	0.714	116.7	114.8	73.4	61.2	19.4 (19.0)
	1500	473.9	0.731	173.1	172.2	73.8	93.4	19.7 (19.4)
6k-PDMS/ PEDOT: PSS	500	158.0	0.697	59.7	58.6	73.6	30.5	19.3 (19.0)
	1000	315.9	0.715	118.6	117.2	74.0	62.8	19.9 (19.4)
	1500	473.9	0.732	178.4	175.8	74.3	97.0	20.5 (20.0)
10k-PDMS/ PEDOT: PSS	500	158.0	0.694	57.6	56.3	72.2	28.9	18.3 (17.8)
	1000	315.9	0.710	114.5	112.7	73.3	59.6	18.9 (18.3)
	1500	473.9	0.727	170.3	169.0	74.0	91.6	19.3 (18.9)